The Astrophysical Journal, 646:593–604, 2006 July 20

THE EVERSHED FLOW: FLOW GEOMETRY AND ITS TEMPORAL EVOLUTION

T. Rimmele and J. Marino
National Solar Observatory, Sunspot, NM 88349; rimmele@nso.edu
Received 2006 February 23; accepted 2006 March 24

ABSTRACT

A diffraction-limited 120 minute time sequence of Evershed flows along penumbral filaments was obtained using high-order adaptive optics in conjunction with postprocessing. We observe individual Evershed flow channels and study their evolution in time. The vast majority of flow channels originate in bright, inner footpoints of size 0.″2–0.″4 with an upflow. The upflow turns into a horizontal outflow along a dark penumbral filament within fractions of 1″ (300–500 km). The time sequence clearly shows that both (bright) upflow and (dark) horizontal flow move around and evolve as a unit, indicating that they are part of the same feature. The inner footpoints are brighter than the average quiet photosphere and move inward at 0.5–1 km s^{-1}. Our observations provide strong evidence that penumbral grains are the inner footpoints of Evershed flows where a hot upflow occurs. We observe an Evershed flow channel as it appears to emerge near the outer penumbra and track the flow over a period of about 100 minutes as it moves toward the penumbra-umbra edge, where it disappeared. We observe a steep decline ($\leq$0.″2) of the velocity at outer end of individual flow channels, even for flow channels that end well within the penumbra. This sharp outer edge of the flow channels is also observed to move inward toward the penumbra-umbra boundary. Flows in dark-cored penumbral filaments appear to be produced by the Evershed effect. We discuss our observational results in the context of models of the Evershed effect. Some aspects of our observations provide strong support for the moving tube model of the Evershed flow.

Subject headings: sunspots — Sun: atmospheric motions — Sun: magnetic fields

1. INTRODUCTION

Sunspot penumbra still present many mysteries to solar astronomers. In particular, the complex magnetic field structure and the dynamic evolution of penumbral fine structure is not yet well understood. (See recent review articles by Thomas & Weiss [2004] and Weiss [2006] for a summary of outstanding problems concerning the physics of the penumbra.)

The penumbral magnetic field is highly inhomogeneous. Several observations performed over the last decade have shown that the inclination of the field vector is different in dark and bright filaments (Title et al. 1993; Lites et al. 1993; Solanki & Montavon 1993). The magnetic field is generally more vertical in bright filaments. In particular, this is true near the outer penumbra, where dark filaments are found to be nearly horizontal, and the difference in inclination angle between the more vertical bright filaments and nearly horizontal dark filaments can be 30°–40° (Langhans et al. 2005).

Based on these observations, the picture of an interlocking-comb magnetic field structure, sometimes also referred to as "uncombed" or "fluted" penumbra, has now been generally accepted as an accurate description of the penumbral magnetic field geometry. (For a comprehensive discussion of this subject see Thomas & Weiss [1992, 2004], Solanki [1993, 2003], or Weiss [2006].) This intuitively rather unexpected field geometry has been referred to as "the most remarkable feature of sunspot magnetic fields" (Thomas & Weiss 2004).

The extensively studied Evershed flow (Evershed 1909) is an important aspect of penumbral physics that must be explained by any successful penumbral model (see, e.g., Thomas & Weiss 2004). It is also considered a firmly established fact that the Evershed flow occurs along magnetic field lines (Bellot Rubio et al. 2003; Borrero et al. 2004), as fundamental physics would dictate, if the Evershed effect is indeed caused by a plasma flow. The correlation between Evershed flow and dark and bright filaments has been somewhat controversial among observers. The early observations of Beckers & Schröter (1969) found the Evershed effect co-located with dark filaments. Other observers did not find a clear correlation between Evershed flow and dark filaments (Wiehr & Stellmacher 1989; Lites et al. 1990). Although, a number of more recent high-resolution observations seem to provide strong evidence that the Evershed flow is predominately co-located with the horizontal, dark filaments (e.g., Title et al. 1993; Langhans et al. 2005). This correlation is generally stronger when velocity and intensity signals that form at approximately the same height in the atmosphere are compared (Rimmele 1995a, 1995b; Stanchfield et al. 1997). Schlichenmaier et al. (2005) find that the correlation between dark filaments and Evershed flow varies from the center-side to the limb-side penumbra and high correlation coefficients are found only locally. They conclude that the Evershed flow occurs in bright and dark filaments.

The Evershed flow is time dependent. Flow speeds along flow channels vary on timescales of 10–20 minutes (Rimmele 1994; Shine et al. 1994). It has been argued that since these velocity variations are observed to be coherent across several individual flow channels, it could mean that they are produced by larger scale wave motions and are not an inherent feature of the actual Evershed flow along individual flux tubes (Thomas & Weiss 2004).

Theoretical models of the Evershed effect include the siphon flow model (Thomas & Montesinos 1993, 1997; Montesinos & Thomas 1998) and the moving tube model (Schlichenmaier et al. 1998a, 1998b).

A siphon flow develops along a magnetic loop, the footpoints of which have different magnetic field strength (at the same geometrical height). The resulting pressure difference between the two footpoints of a penumbral flux tube is what drives the Evershed flow.

Schlichenmaier et al. (1998a, 1998b) model the dynamic evolution of a thin flux tube inside the penumbra. A flux tube initially

located at the magnetopause becomes buoyant due to radiative heating and rises. Radiative cooling at the photosphere produces pressure differences along the loop, driving an outward-directed flow along the flux tube as it rises through the penumbra. Thomas & Weiss (2004) point out that the outflow produced by the moving tube model is also the result of a gradient in gas pressure and requires or leads to higher magnetic field strength at the outer footpoint as well. The moving tube model assumes that at the outer edge of the penumbra flow continues along the magnetic canopy where an open boundary condition is applied.

The moving tube model predicts (see Fig. 8 of Schlichenmaier et al. 1998a) a filament structure that is characterized by a hot, nearly vertical upflow of hot plasma at the footpoint of the filament, which within a few 100 km turns into a horizontal filament that is elevated by $\sim$100 km above the surface. Schlichenmaier et al. discuss observational consequences of their model. At the footpoint the tube's temperature is higher than the corresponding background values, and the footpoint appears bright. They point out that the footpoint of the flux tube inside the penumbra could therefore be identified with a bright penumbral grain. It has also been suggested that these hot upflows may significantly contribute to the heating of penumbra (Schlichenmaier & Solanki 2003). As the plasma flows along the tube, it looses energy by radiation and cools off, and the filament becomes as dark as its surroundings. Rimmele (2004a) observed flows along penumbral filaments that seem to confirm at least some aspects of the Schlichenmaier et al. (1998a, 1998b) model.

Inspired by the discovery of dark-cored penumbral filaments (Scharmer et al. 2002), Spruit & Scharmer (2006) have taken a new look at penumbral structure. The authors propose that penumbral filaments are due to convection in field-free, radially aligned gaps just below the visible surface of the penumbra. The model produces a horizontal magnetic field at some height above the gap, producing an environment in which the Evershed effect could occur. However, the authors do not claim that the model provides a satisfactory explanation for the Evershed effect.

Although we did not perform direct measurements of magnetic field, the highly resolved observations of penumbral flows, and in particular their temporal evolution over an extended period of time, presented here do provide important clues that will aid in the interpretation and development of realistic penumbral models. For example, our observations provide strong evidence in favor of some aspects of the moving tube model.

2. OBSERVATIONS

The observations were performed on 2004 May 6 at the 76 cm Dunn Solar Telescope (DST) in Sunspot, NM. We observed a relatively round sunspot (NOAA 0605) positioned at 12° south, 23° west at a position angle of $\cos\Theta = 0.86$. The tunable universal birefringent filter (UBF) was used to obtain a time sequence of Dopplergrams and narrowband filtergrams. The UBF was tuned into the red and blue wings (offset $\pm$100 mÅ), respectively, of the spectral line Fe I λ5576, which in the penumbra forms at an altitude of about 240 km (Bruls et al. 1991). The "nonmagnetic" Fe I λ5576 line (effective Lande-factor $g = 0$) provides a Doppler signal free of any cross talk from the magnetic field. At this wavelength the UBF has a passband of about 145 mÅ. Because of the broad filter passband, the measured wing intensities are averages over large portions of the wing profile. Hence, the Dopplergrams give a measure of the mean position of the spectral line. Obviously, any information about vertical gradients in the velocity field is lost due to the coarse spectral resolution. However, this velocity is relatively insensitive to changes of the spectral line profile and line parameters such as line strength and line width that have been observed to occur on filamentary scales in the penumbra (Rimmele 1995a, 1995b; Tritschler et al. 2004).

UBF filtergrams were recorded with a 1k $\times$ 1k CCD camera with a pixel resolution of 0.″025 pixel^{-1}, i.e., highly oversampled. The diffraction limit at 5576 Å is $\lambda/D = 0.''15$. The field of view (FOV) of the UBF was approximately 25.″ The exposure time was set to 1.2 s. We collected data over a period of about 118 minutes, during which the seeing conditions were good but variable.

The high-order adaptive optics system (Rimmele 2004b) was deployed to correct for the majority of atmospheric seeing. However, variable seeing conditions result in a variable degree of correction of the adaptive optics system and hence in variations of the PSF observed at the detector plane. In order to alleviate the negative impact of these residual seeing effects, we used a method that allows the estimation of the long-exposure point-spread function (PSF) from the adaptive optics wave front sensor telemetry. An "instantaneous" PSF can be derived strictly simultaneous with each UBF exposure. The method was originally developed for application to point sources and curvature-sensing adaptive optics systems (Véran et al. 1997) and has been modified for use with the extended-source solar adaptive optics system deployed at the DST (Marino et al. 2004).

3. DATA REDUCTION

After flat-field and dark correction the UBF filtergrams were corrected for small amounts of residual differential image motion that were visible across the extended FOV by using a destretch algorithm. We computed a total of 286 Dopplergrams (line-of-sight [LOS] velocity maps) in the usual manner,

$$\text{velocity} = c_v \times \frac{I_{\text{red}} - I_{\text{blue}}}{I_{\text{red}} + I_{\text{blue}}}. \quad (1)$$

The Dopplergrams were calibrated using a calibration factor (c_v) determined by modeling the spectral profile of the observed lines as observed through the UBF. The Liege atlas profile was convolved with the UBF passband, from which the calibration factor can be derived directly. Blue- and red-wing filtergrams were added to produce an intensity map corresponding to approximately the same height as the velocity map. The effective exposure time for both velocity and intensity maps is therefore 2.4 s. The average umbral velocity was chosen as the velocity reference point (see Rimmele 1995b).

The principle of the long-exposure PSF estimation is as follows. In closed loop the adaptive optics (AO) system applies a correction to the aberrated incoming wave front using a deformable mirror (DM). However, because of the limited spatial and temporal resolution of both the DM and wave front sensor (WFS), correction can only be partial. After reflection off the DM any residual wave front errors are measured with the WFS. These residuals give a good indication of the actual performance of the AO system and the degree of correction achieved for wave front sensor modes that the AO system attempted to correct. The impact of the residual wave front errors on the PSF can be quantitatively estimated.

Furthermore, because of the finite number of WFS subapertures, spatial modes with spatial frequency higher than that of the highest correctable mode will traverse the AO system undetected and therefore remain uncorrected. The impact of these unseen modes on the PSF can be estimated with knowledge of the Fried parameter r_0, which can be estimated from the statistics of the actuator commands that are applied to the DM. This assumes Kolmogorov seeing statistics, which, through wave front sensor

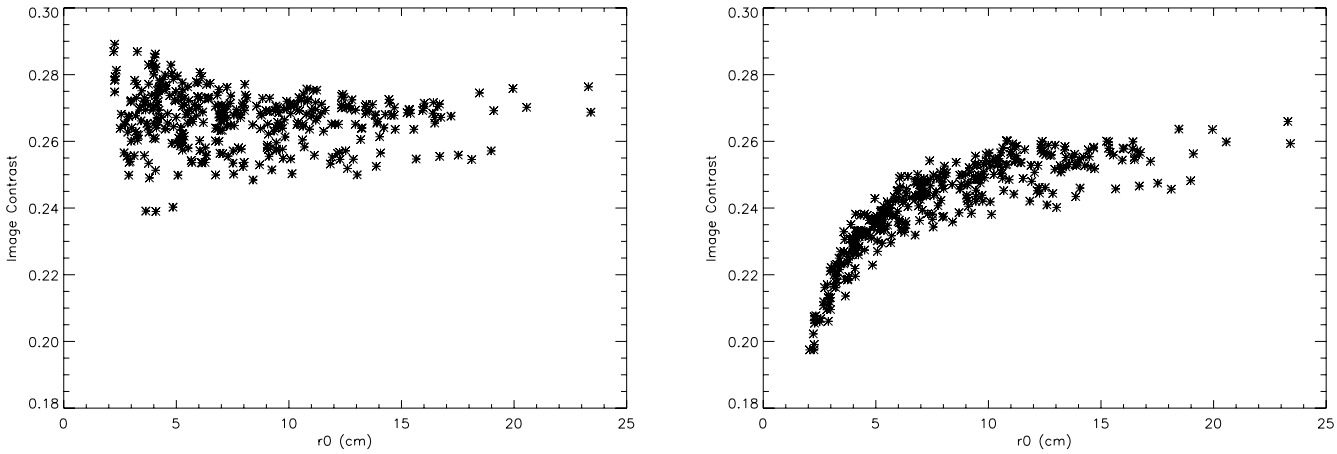

FIG. 1.—Image contrast of UBF sunspot filtergrams as a function of the Fried parameter r_0 for uncorrected images (*left*) and after deconvolution with estimated PSFs (*right*).

measurements, have been found to accurately describe atmospheric turbulence above the Sacramento Peak (New Mexico) site. In addition to the uncorrected residuals and uncorrected higher order modes, noise sources such as aliasing noise and wave front sensor noise have to be taken into account. All this information is combined to provide an estimate of the PSF. The method and the results of verification experiments performed with point sources are described in detail by Marino et al. (2004). The PSF is used to deconvolve the corresponding UBF filtergrams using a simple Wiener filter. Through this process the amplitudes (contrast) of the images can be recovered within the stated accuracy. This is of particular importance for the Dopplergram observations performed for this study. Since the filtergrams that are combined to generate a Dopplergram are not taken simultaneously, variations in the PSF between the subtracted filtergrams can cause spurious velocity signals.

Using the PSF estimation technique, we were able to produce a consistent, high-resolution time sequence of filtergrams and Dopplergrams in spite of variable seeing conditions. Figure 1 plots the image contrast of the filtergrams as a function of the Fried parameter as observed (*left*) and after deconvolution with the estimated PSFs (*right*). The contrast of the "raw" sunspot filtergrams shows a strong dependence on r_0, in particular for Fried parameters $r_0 \leq 7$ cm. This deterioration of AO performance (Strehl ratio) for small Fried parameters is expected since the WFS subaperture size is 7.5 cm. In the deconvolved sequence, the contrast curve is flat, indicating that the PSF estimation accurately recovers the amplitudes over a wide range of seeing conditions. However, the plot also indicates that for small Fried parameters the reconstruction becomes more noisy.

A temporal low-pass filter was applied to the time sequences of filtergrams and Dopplergrams in order to remove fast (e.g., 3, 5 minutes) oscillatory components that are definitely visible in the time sequences. The goal was to study the long-term evolution of the Evershed flow. The filter therefore passes frequencies $\leq$2 mHz. It has been shown that the Evershed effect evolves within 10–20 minutes (Rimmele 1994; Shine et al. 1994), timescales which are well within the applied filter.

The statistical errors in the Doppler measurements can be estimated from the photon noise in the filtergrams and the equation given above and because the large number of photons collected (long exposure) are of order 20 m s^{-1} only. Although the adaptive optics greatly reduces seeing effects, the dominant error source in the uncorrected and unfiltered Dopplergrams remains residual seeing effects. These random errors can be estimated from the difference of consecutive Dopplergrams. Because of the fast cadence, we do not expect significant change of the penumbral structure, i.e., the difference signal is mostly due to residual seeing effects. The random errors are of order 65–80 m s^{-1}. These relatively small random errors are reduced further to about 15 m s^{-1} by applying the PSF deconvolution and the temporal filter.

4. RESULTS

Figure 2 displays a sample narrowband filtergram and the corresponding Dopplergram. In spite of the long exposure time, the resolution of both intensity and velocity maps is excellent and approaches the diffraction limit. Bright points as well as umbral dots are visible in the filtergrams. This demonstrates the effectiveness of the real-time adaptive optics correction combined with the ex post facto PSF correction.

It has been well established that the Evershed flow is mostly horizontal, i.e., parallel to the solar surface (see Thomas & Weiss 2004 and references therein). Since the spot was observed away from disk center, we observe the typical Evershed flow pattern that is characterized by redshifted spectral profiles in the limb-side penumbra (Fig. 2, *top left corner of bottom panel*) and blueshifted profiles in the center-side penumbra (*bottom right corner of bottom panel*). The measured maximum velocities range between +2 and −2 km s^{-1}. Assuming a perfectly horizontal flow and taking into account projection effects ($\sin\Theta = 0.5$), this amounts to a flow amplitude of about 4 km s^{-1}. Previous publications quote Evershed velocities of up to 6 km s^{-1}. However, we have to consider the broad filter bandpath and the resulting averaging over large potions of the spectral-line wings, which will lower inferred velocity amplitudes compared to bisector velocities from high spectral resolution data.

The limb-side penumbra allows one to distinguish between upflow (blueshift) that one would expect to observe at the inner footpoints of Evershed loops and outflow (redshift) along the nearly horizontal magnetic flux tube. In the center-side penumbra both flow components would appear blueshifted and are not easily distinguished in simple LOS Dopplergrams. We therefore focus our further analysis on the limb-side penumbra.

4.1. *Evershed Flow Geometry along Individual Filaments*

Figure 3 shows velocity and intensity maps of a portion of the limb-side penumbra. The most striking features seen in the velocity map are the small-scale (0.″2) upflows located at the

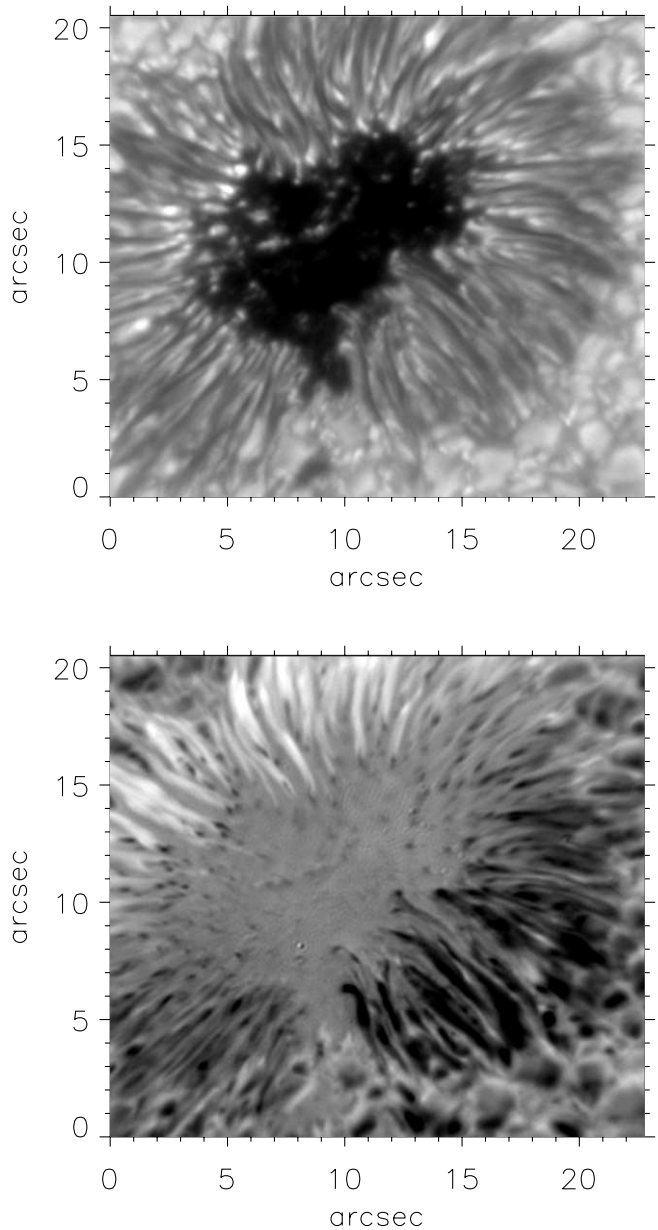

FIG. 2.—Narrowband filtergram and Dopplergram of a sunspot observed at approximately 30° away from disk center. The effective exposure time was 2.4 s. The Dopplergram shows the signature of the Evershed flow. The solar limb is toward the top left corner of these images. The velocities are encoded in a gray scale. *Bright:* redshift; *dark:* blueshift.

inner footpoints of a flow channel. Close inspection reveals that upflows can be identified at the inner footpoint for most if not all of the observed flow channels. Comparing intensity and velocity maps, it can be seen that upflows are co-located with bright features often referred to as penumbral gains, while the horizontal, redshifted outflow is correlated with a dark filament. This correlation persists throughout the entire time sequence. Complex, twisted and entangled flow channels make a clear association more difficult (but not impossible). Hence, we select a few flow channels that can be easily identified as individual filaments and trace their velocity and intensity signals in the radial direction, i.e., along the axis of a filament, and across several filaments in the azimuthal direction.

Figure 4 shows representative examples of such traces from different time steps in the sequence. The azimuthal trace clearly shows that redshifted flows are correlated with dark filaments. The radial traces start at the inner penumbral footpoint and reveal the close correlation between upflow and "bright grain" as well as the correlation between horizontal flow and dark penumbral filaments. The intensity of the bright points usually exceeds the average brightness of the surrounding "quiet" photosphere. Values in the range of $I = (1{-}1.2)I_{\rm quiet}$ are observed. The spatial extent of the footpoints along the filament axis can be inferred from Figure 4 and is of order $\leq 0\farcs4$ FWHM. Another striking feature is the very steep rise of the velocity signal from blueshift to redshift. The intensity signal changes from bright to dark over a similar distance. As a measure of the distance over which the flow turns from vertical to horizontal (bright to dark), we measure the distance between the location of the maximum upflow and the point where the redshift only increases gradually. This distance is between $0\farcs5$ and $0\farcs7$ or 380–500 km.

After the initial steep rise, the velocity increases only very gradually along the radial direction until, at the outer boundary of the flow channel, which is usually located near the outer edge of the penumbra, an even steeper decline of the velocity is observed. The length of the flow channels in the radial direction for different filaments ranges from 2″ to 6″ (1500–4500 km) as measured from the maximum upflow to the half-point of the velocity drop of at the outer edge. In a very few cases unusually short and short-lived filaments were observed (see Fig. 7).

4.2. *Flows in Dark-cored Penumbral Filaments*

The resolution in our observations is good enough to identify dark-cored penumbral filaments (Scharmer et al. 2002) in the filtergrams and to study the corresponding flow pattern. The observational signature of dark-cored filaments is a narrow dark line in the center of bright filaments extending along the axis of the filament. Dark-cored filaments are often seen in the inner penumbra and are more easily identified in the center-side penumbra (Sütterlin et al. 2004), suggesting that they are shallow features (Weiss 2006).

Figure 5 shows scaled-up images of a small section of the inner penumbra that contains what we believe are dark-cored penumbral filaments. We show examples from both the limb-side and center-side penumbra. The corresponding velocity map is shown as well.

These images provide strong evidence that dark-cored penumbral filaments originate at bright footpoints near the penumbra-umbra boundary. The footpoints are co-located with upflows, while the dark-cored filaments are co-located with redshift. The dark cores appear to be the signatures of well-defined individual flow channels. We stress again that the dark portion of the filament is associated with the more horizontal outflow, which is usually referred to as the Evershed flow. Figure 5, and in particular, the temporal evolution of these flows and their corresponding intensities, which are discussed in the following section, provide strong evidence that bright grains and dark cores belong to the same flow system along a magnetic loop, i.e., they are both signatures of the Evershed effect.

It is not entirely clear whether the examples of dark-cored filaments shown from the limb-side penumbra fit the definition given above as well as the examples from the center-side do. However, the flow pattern measured along the dark cores is very similar in the center-side and limb-side penumbra. The line plot in Figure 5 shows a trace along a dark-cored filament from the center-side penumbra. Here we also clearly see a bright, blueshifted feature at the inner footpoint of the flow channel. Instead of the quick turn to redshift observed in the limb-side penumbra

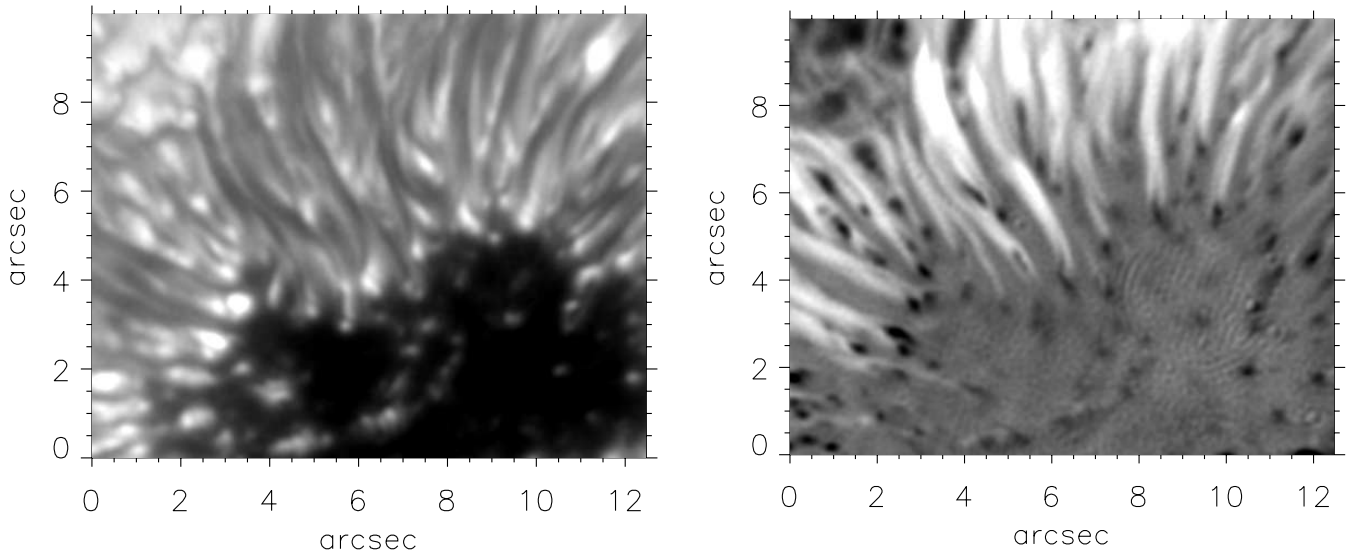

FIG. 3.—Dopplergram and filtergram of limb-side penumbra. In the Dopplergram, dark and bright areas mark blueshifted and redshifted line profiles, respectively.

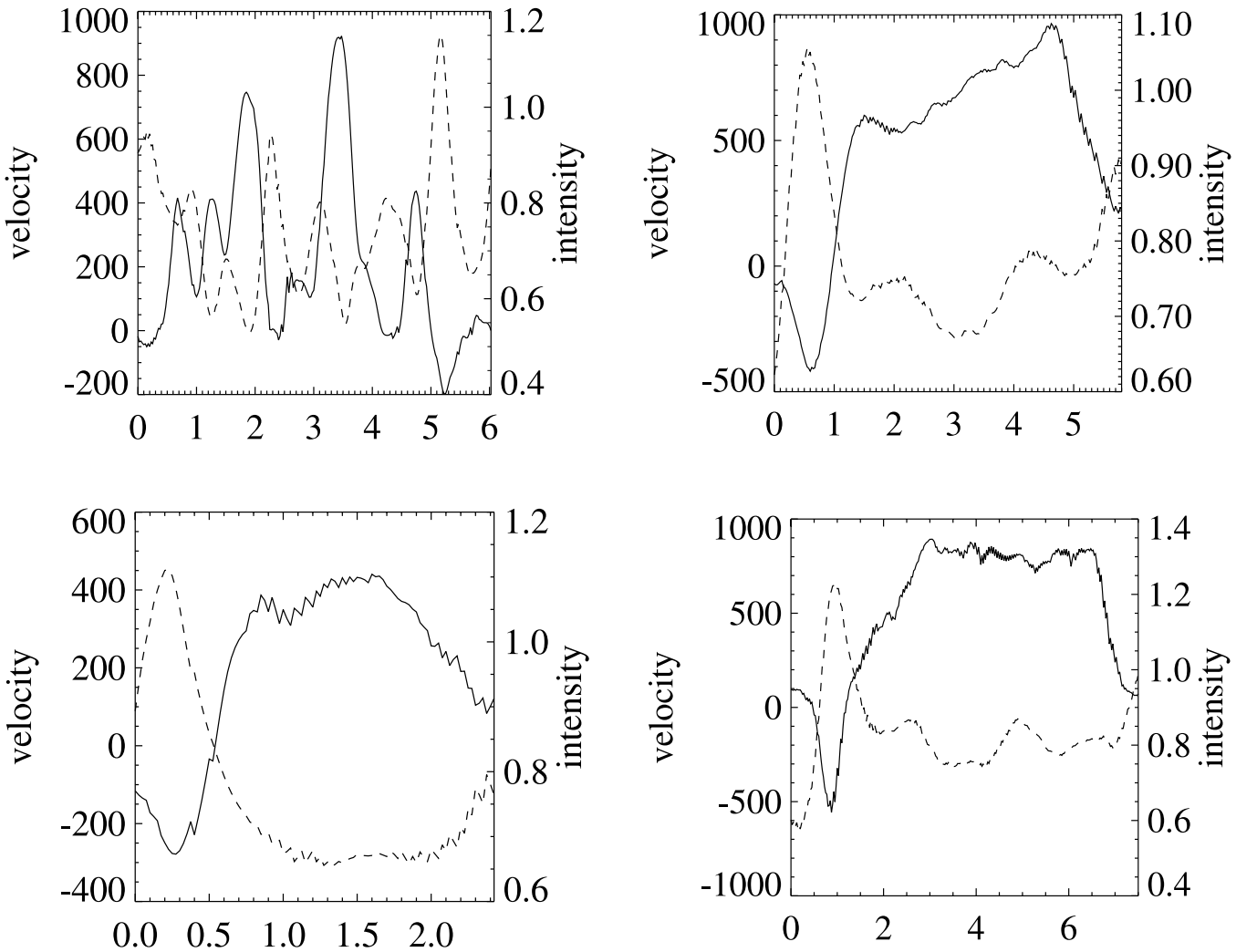

FIG. 4.—Velocity (*solid line*) and intensity (*dashed line*) traced across several filaments in the azimuthal direction (*top left panel*) and along several filaments in the radial direction (*top right and bottom panels*). Positive velocity corresponds to redshifted line profiles. Note the strong correlation between upflow and bright point as well as the steep decrease of the velocity near the outer penumbra.

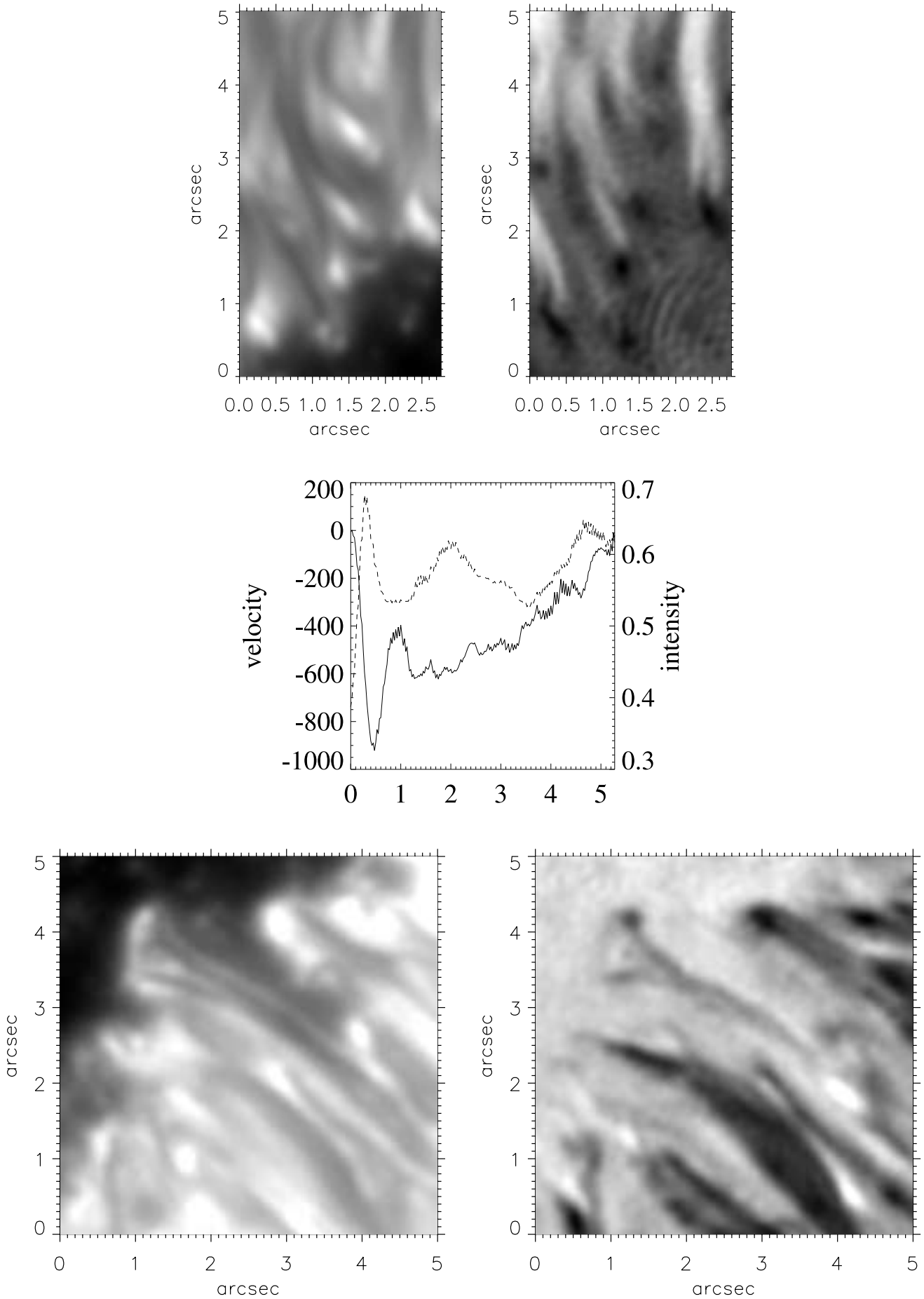

FIG. 5.—Close-up view of dark-cored penumbral filaments. *Left:* intensity; *right:* velocity. Examples from the limb-side (*top*) and center-side penumbra (*bottom*) are shown. The artifacts seen in the velocity map of the top right panel are from an imperfect flat-field correction. The line plot shows a trace along a dark core in the center-side penumbra. *Solid:* velocity; *dashed:* intensity. The plot demonstrates that the bright inner footpoint of the flow channel is also seen for the center-side penumbra.

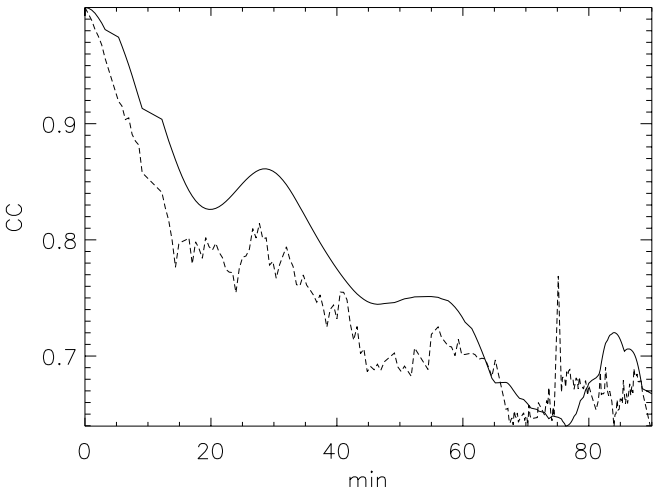

FIG. 6.—Maximum of two-dimensional cross-correlation as a function of time of velocity (*solid line*) and intensity (*dashed line*) maps seen in Fig. 3. Note the secondary and tertiary maxima at about 30 and 55 minutes, respectively.

(Fig. 4), the velocity remains blueshifted, as would be expected for a horizontal outflow simply because of LOS effects.

We note that there are a number of redshifted areas visible in center-side penumbra. One might be tempted to interpret these downflows as Evershed return flows, which have been reported to exist within the outer penumbra (Westendorp Plaza et al. 1997). However, the downflows seen in Figure 5 are not readily associated with individual flow channels, i.e., as end points (outer footpoints) of the Evershed flows.

4.3. *Temporal Evolution of Evershed Flows*

Before discussing the temporal evolution of Evershed flow channels in detail, we discuss the temporal cross-correlation of the penumbral velocity field. We computed the time sequence of two-dimensional cross-correlation for the FOV shown in Figure 3. All consecutive frames were tracked and correlated to this reference. Figure 6 plots the maximum value of the two-dimensional cross-correlation as a function of time for both intensity and velocity. The plots indicate how the scene decorrelates over time and thus gives an indication of the lifetime of penumbral structures. Low spatial frequencies (general shape of sunspot) decorrelate slowly, which explains the high degree of correlation that persists even after 90 minutes. The rapid decorrelation observed in the first 15–20 minutes followed by a more gradual drop in the correlation can be explained by the evolution of penumbral fine structure.

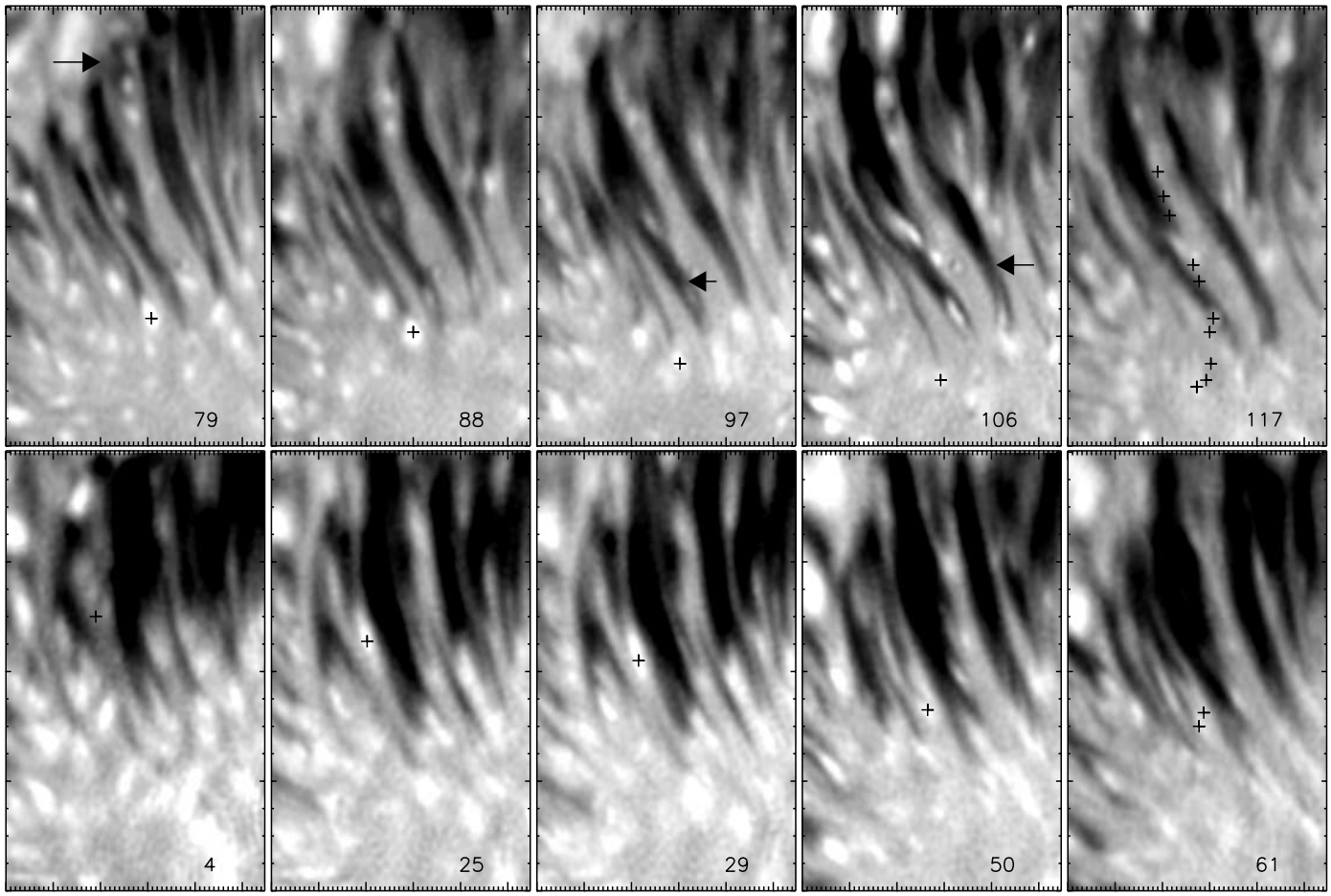

FIG. 7.—Time sequence of velocity maps. The FOV is $5''.5 \times 8''$. The time steps are 4, 25, 29, 50, 61, 79, 88, 97, 106, and 117 minutes. The temporal evolution of a filament from the time when is first becomes visible to the time when it disappears is depicted with these images. The crosses mark the position of the inner footpoint (upflow), which steadily moves inward toward the penumbra-umbra boundary with a proper motion velocity of about 0.5 km s^{-1}. The average proper motion speed can be inferred from the distance the inner footpoint traveled (trace marked by the crosses) divided by the traveling time. The gray scale has been reversed for better showing, i.e., *dark:* redshift; *bright:* blueshift. The arrows point to examples of "crossing filaments." Evidence for unusually short flow channels is seen near the outer penumbra at time step 79 minutes (*arrow*).

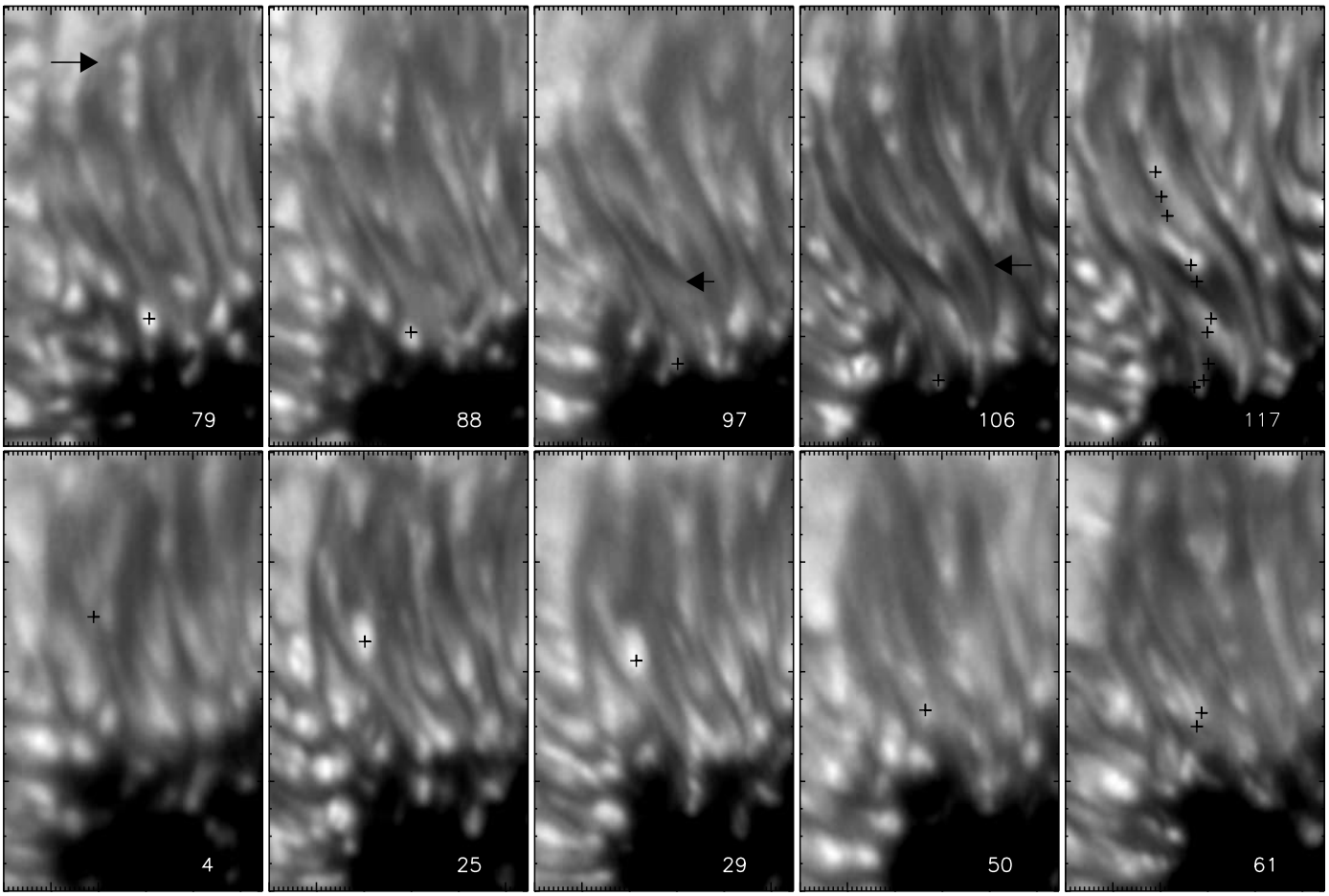

Fig. 8.—Time sequence of intensity maps corresponding to velocity maps shown in Fig. 7.

An interesting feature of these cross-correlations is the secondary and tertiary maxima at about 30 and 55 minutes, respectively. These maxima are clearly visible in the velocity correlation and less prominent in the intensity correlation. These secondary and tertiary maxima might be the signatures of recurring Evershed flow packages observed by Rimmele (1994) and Shine et al. (1994).

Figures 7 and 8 show a time sequence of Doppler maps and corresponding intensity maps. A small $5''.5 \times 8''$ FOV was selected in order to highlight at high spatial resolution the evolution of a few representative penumbral filaments. We attempted to follow flow channels throughout their entire life cycle. A particularly nice example is marked in this sequence of velocity and intensity images. A flow channel first appears in an area that shows what appears to be a small-scale convective pattern penetrating into the outer penumbra. The crosses mark the position of the inner footpoint of the flow channel. Immediately after the flow channel appears, the inner footpoint begins to move inward, while during these early stages, the outer boundary of the flow remains more or less in the same position, i.e., the filament becomes more and more elongated. At time step 61 minutes, two footpoints become visible, indicating that either previously unresolved flow channels have split sufficiently to become resolved, or a second flow channel has emerged at this location. Continuing with time step 79 minutes, we observe again a single flow channel, the clearly visible footpoint of which continues to move toward the penumbra-umbra boundary. During these later stages of the evolutionary path of the filament, the outer edge of the flow channel is moving inward as well (see also Fig. 9). Adjacent flow channels behave in a similar fashion. Toward the end of the sequence, the flow channel fades away. The crosses in the last image trace the motion of the inner footpoint from the outer parts of the penumbra to the very edge of the penumbra-umbra boundary. Other flow channels can be observed to undergo a similar evolutionary path. The flow stops (or becomes invisible) as soon as the inner footpoint reaches the umbra or in some cases enters the umbra and becomes what has been refereed to as peripheral umbral grain in the literature (Grossmann-Doerth et al. 1986; Hartkorn & Rimmele 2003).

In Figure 9 we plot traces along the flow channel for two different time steps marking different evolutionary stages of the flow. At the very beginning of the sequence, the blueshifted and redshifted parts of the flow are more balanced in terms of amplitude and spatial extend along the loop. The flow geometry is consistent with an inverse U-loop. As the inner footpoint moves toward the penumbra-umbra boundary, the upflow becomes very localized. As already mentioned earlier, the flow geometry is consistent with an upflow that quickly turns over to a horizontal radial outflow. The outer edge of the flow channel moves inward as well.

It is difficult to determine whether near the beginning of the time sequence an already-existing flow emerges into the photosphere from below or whether the flow forms in a magnetic loop that is already located in the photosphere. Figure 10, which shows the evolution of the velocity along the radial axis of the flow as the flow channel appears, holds a possible clue. The fact that blueshift and redshift appear simultaneously argues in favor of an emerging

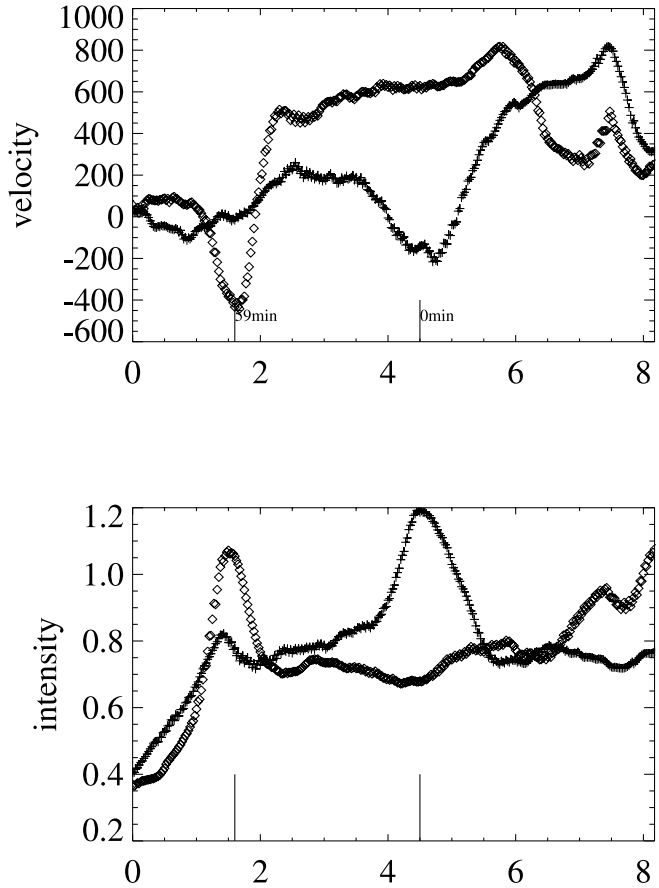

FIG. 9.—Evolution of flow channel. Traces are in the radial direction along the filament axis. *Top:* velocity; *bottom:* intensity. Two different time steps are shown. 0 minutes (*crosses*) refers to shortly after the flow first becomes visible. At 59 minutes (*diamonds*) the inner footpoint has moved close to the penumbra-umbra boundary. The sharp outer edge of the flow channel is seen to move inward as well.

preexisting flow. One would expect a flow that develops along an existing magnetic loop to first exhibit an upflow at the inner footpoint that then propagates outward. In this figure we also find that the location of the maximum blueshift begins moving inward immediately, which is consistent with an emerging loop as well.

4.4. *Stacked Flow Channels*

We were able to identify numerous examples in our data where penumbral flow channels appear twisted and tangled, apparently crossing each other in the azimuthal direction. We find that this is more readily seen in the velocity maps, where individual filaments (flow channels) can be more easily identified and traced. The arrows in Figure 7 point to two examples of where such crossing of filaments (flows) occurs, giving the impression that at the crossing points filaments are stacked on top of each other in the vertical direction. In between flow channels (or clusters of flow channels), we observe areas ("filaments") with velocities close to zero.

The data provide some evidence that at the location where flow channels cross we observe an increased velocity signal. Figure 11 shows an example. We show traces in the radial and azimuthal direction. Near the inner footpoints two individual filaments are clearly resolved. Moving toward the outer penumbra to the location where the flow channels cross, the flows are no longer distinguishable as separate features, whereas near the footpoints the structures are clearly distinguishable. At the crossing point the flow amplitude suddenly increases. This is not surprising, since

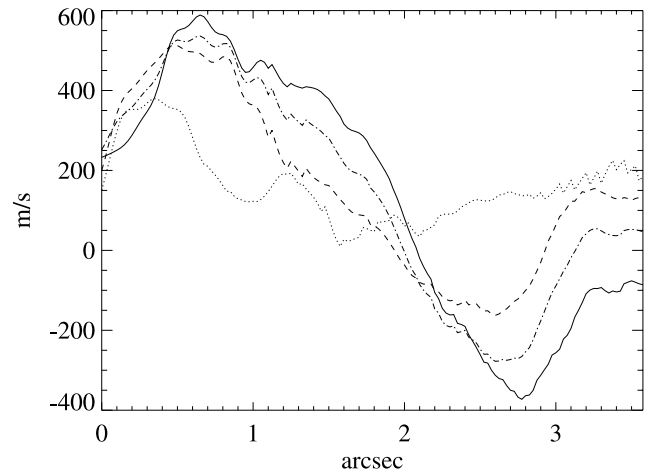

FIG. 10.—Evolution of flow channel marked in Fig. 7 during early stages. The velocity traces are in the radial direction along the filament axis. The time steps are 0 minutes (*dotted*), where the Evershed flow is not yet visible, 16 minutes (*dashed*), 19 minutes (*dash-dotted*), and 24 minutes (*solid*). The inner footpoint (upflow) begins to move toward the inner penumbra immediately, whereas the outer edge during this early phase stays in place.

two flow channels, stacked on top of each other, fall within the response function of line, i.e., the "velocity fill factor" increases in both the vertical and the horizontal direction. It would be interesting to obtain observations of crossing filaments with significantly higher spectral resolution in order to study the line profiles and bisectors. One would expect to see more complex bisector shapes at locations where two (or more) flow channels, located at different heights in the atmosphere, fall within the line response function. Unfortunately, because of the broad filter bandpath of the UBF our data are not suited to provide bisector information.

5. SUMMARY AND DISCUSSION

The main observational results can be summarized as follows.

1. Individual Evershed flow channels can be identified. The lateral extent of the flow channels is very near the diffraction limit of the telescope ($\leq 0\farcs2$), and we expect the actual size of the flow to be even smaller.
2. Flow channels often seem to cluster together, forming a conglomerate of what appears to be twisted and tangled flow channels that in many cases cross each other at different heights is the atmosphere. One might also call this "uncombed" penumbral structure. Penumbral fine structure appears to be even more complex than the already surprisingly complex, widely accepted interlocking-comb structure would suggest.
3. In between flow channels (or clusters of flow channels) we observe areas ("filaments") with velocities close to zero.
4. For the vast majority of Evershed flow channels, an inner footpoint can be identified. This inner footpoint is a small ($\leq 0\farcs2$), pointlike, bright upflow that has all the characteristics of what has been dubbed "bright penumbral grain" in the literature, i.e., penumbral grains are the inner footpoints of Evershed flow channels. The plasma flow vector, expected to be field aligned (Bellot Rubio et al. 2003), is more vertical in bright upflowing regions that mark the inner footpoints of the Evershed flow.
5. The intensity of the bright points generally exceeds the average photospheric brightness.
6. The upflows observed in the bright footpoint turns over to a nearly horizontal flow within a very short distance ($0\farcs5$–$0\farcs7$ or 380–500 km). This horizontal part of the flow is correlated with a dark filament or dark-cored filament.

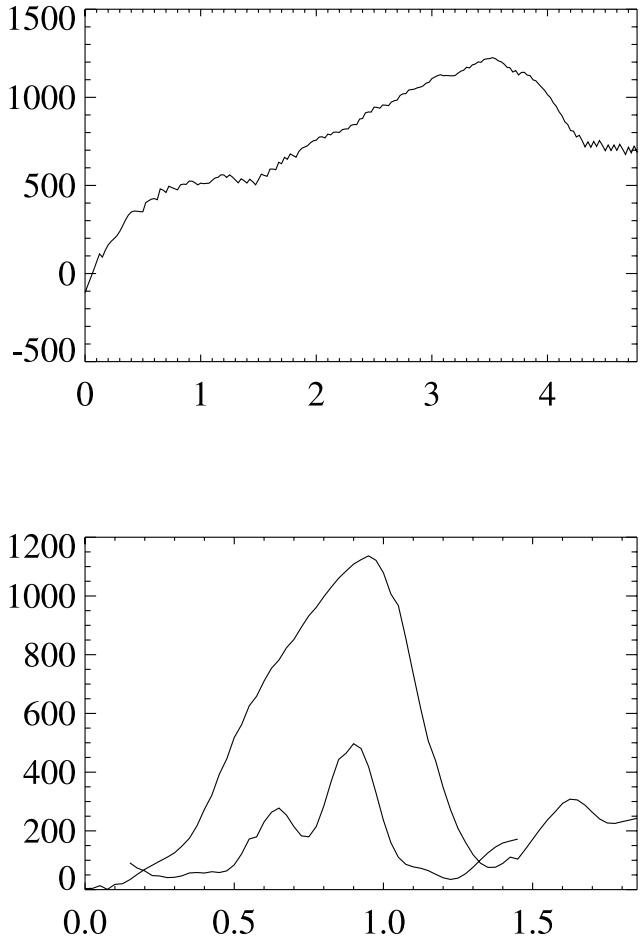

FIG. 11.—Evidence for crossing flows. *Bottom:* Trace across two individual flow channels near their footpoints, where the channels are resolved, and at the point where the two filaments appear to cross in azimuthal direction and at different heights. *Top:* Trace in along one of the flow channels. At the location where the flow channels cross, a sudden increase in flow velocity is observed.

7. In the limb-side penumbra the LOS component of the upflow is of order 300–500 m s^{-1}. In the center-side penumbra we observe LOS upflow velocities of order 1000 m s^{-1}.

8. We observed an extremely steep decline of the velocity at the outer end of the individual flow channels. It is interesting to note that this sharp drop-off of the Evershed flow is not only found at the outer edge of the PU, but flow channels that end well within the penumbra (even the inner PU) also exhibit this rapid decay over, in some cases, less than 0.″2.

9. We were able to study the temporal evolution of individual flow channels and trace them from first appearance to their disappearance. While undergoing significant changes, individual flow channels could be traced as they move from the outer parts of the penumbra to the penumbra-umbra boundary, where the flow disappears. The proper motion speed was determined by tracking the upflow at the footpoint (see Fig. 7 legend) and is of order 0.5–1 km s^{-1}, consistent with previous measurements of penumbral grain motion (e.g., Sobotka & Sütterlin 2001).

10. The bright, inner footpoint and the dark filament carrying the horizontal outflow are observed to evolve as a unit. This indicates that dark filaments and bright grains are part of the same magnetic flux tube that carries the Evershed flow.

11. In the early stages of the flow channel's evolution, the sharp outer edge of the flow channel appears stationary, while during the later stages, the outer edge is observed to also move inward toward the penumbra-umbra boundary. Often this outer edge is located well within the penumbra.

12. A flow channel was observed to emerge from a convective pattern near the outer penumbra. The emerging flow is "archlike" (inverse U). As the flow moves inward, and in particular near the penumbra-umbra boundary, the flow geometry is characterized by the quick turn from upflow to horizontal flow over a very short distance.

13. The length of the majority of flow channels varies between 1500 and 4500 km. A few examples of much shorter loops were observed in the outer penumbra.

14. The lifetime of flow channels ranges from 30–115 minutes.

15. Several redshifted (downflow) areas are found in parts of the center-side penumbra (where the Evershed effect produces blueshift). However, an interpretation of these downflows as Evershed return flows is not obvious from these data.

Many aspects of our observations provide strong support for the moving flux tube model (Schlichenmaier et al. 1998a, 1998b;). The observed flow geometry (upflow in a bright inner footpoint that quickly turns over into a nearly horizontal flow along a dark filament) is consistent with predictions of this model. We also find evidence of Evershed flow channels emerging (rising) from below. However, we consider the most important observation to be the fact that the bright, inner footpoint and the dark filament carrying the more horizontal outflow are moving and evolving as a unit, which in our mind provides convincing evidence that dark filaments and bright grains are part of the same moving magnetic flux tube that carries the Evershed flow. The Evershed flow is associated with both bright and dark penumbral features. The observed movement of the inner footpoints of those flow channels toward the penumbra-umbra boundary with a velocity of about 0.5–1.0 km s^{-1} is also expected in the moving tube model. We note that the timescales predicted by the moving tube model for the rise of a penumbral flux tube (120 minutes) are consistent with the ones observed here.

In order to estimate the actual upflow velocity at the inner footpoints of the flow channels, we assume that the inclination of the flow vector at the inner footpoint is between 35° and 40°, which is the inclination measured for the strong magnetic field component by, e.g., Borrero et al. (2004) and Langhans et al. (2005). Taking into account the sunspots position on the disk (LOS angle), we obtain an upflow amplitude of 0.5–1.5 km s^{-1} in the bright footpoints seen in the limb-side penumbra. It turns out that for the particular observing position of the sunspot on the solar disk in the center-side penumbra, no LOS correction is necessary, i.e., the LOS is such that the actual upflow amplitude is observed in the center-side penumbral grains. In the example of Figure 5 the flow amplitude is 950 m s^{-1}. These upflows are significantly slower than predicted by both the moving tube model, which predict velocities around 3 km s^{-1} at the footpoint (Schlichenmaier et al. 1998a) and the siphon flow model. The horizontal outflow amplitudes we measure are lower as the ones predicted by these models as well. The discrepancy might be explained by still insufficient spatial resolution and the definitely insufficient spectral resolution.

Heating of the penumbra by hot upflows along magnetic flux tubes has been suggested as a mechanism sufficient to explain the penumbral brightness (Schlichenmaier & Solanki 2003). However, Spruit & Scharmer (2006) argue that these upflows are unlikely able to provide the uniform heating of the penumbra along its length.

The occurrence of downflows associated with Evershed flow channels is not obvious at all in our data. This is somewhat

inconsistent with the findings of bisector analysis of the same spectral line (λ5576) by Schlichenmaier et al. (2004), who concluded that downflows in deep layers can explain line asymmetries. We again point to the poor spectral resolution of our observations that, combined with the formation height of the line (mid–upper photosphere), may prevent us from detecting flows deep in the atmosphere.

The interpretation of our observations in the context of alternative models of the Evershed effect is less straightforward. Siphon flow models are stationary solutions and therefore are inherently unable to explain the temporal evolution and proper motion of the flow channel, which we find is common to the vast majority of Evershed flow channels.

We consider it difficult to reconcile our observations with the penumbral model recently put forward by Spruit & Scharmer (2006). As mentioned in the introduction in this model, the Evershed flow is located along horizontal magnetic field structures above the field-free gap. However, the flow can only be carried over a finite distance, i.e., the model is allowing for flows that are rather local and transient. The authors therefore suggest that a local version of the moving tube model might be at work. They further suggest that even though on average the Evershed flow may appear smooth and steady, it is in fact a locally transient phenomena. However, our observations suggest that a more global version of the moving tube model is responsible for the Evershed effect. We find flows that are consistent with the predicted flow geometry and extend over and propagate across large parts of the penumbra. There is a single well-defined inner footpoint, and the lifetime of the flows can be as much as 2 hr. It seems unlikely that these observational signatures could be produced by a local phenomenon. We note that the hyperstructure of dark-cored filaments can be explained by uncombed penumbra models, i.e., can be produced by a nearly horizontal flux tube embedded in a more vertical background field (J. M. Borrero 2006, in preparation).

Although the definition of a dark-cored filament is rather subjective, we find that dark-cored filaments are more readily identified near the penumbra-umbra boundary in center-side penumbra, which agrees with previous observations (Borrero et al. 2004; Sütterlin et al. 2004; Langhans et al. 2005). The dark-cored filaments we identified as such in both the limb-side and center-side penumbra can be associated with regular Evershed flow channels originating in a hot upflow. This is consistent with Bellot Rubio et al. (2005), who find flows in dark-cored filaments to be mostly horizontal with a small upflow component. Interestingly, we find that for our data set a clear identification of bright and dark filaments is difficult for the limb-side penumbra and much more easily performed for the center-side penumbra.

We consider it still a major challenge to explain the sharp ($\leq 0\farcs2$) outer boundary of the Evershed flow. The fact that we see this sharp decline in velocity not only at the penumbra-quiet Sun boundary but throughout the penumbra argues that this effect is not linked to the transition between the magnetic and the nonmagnetic environment. If the sharp boundary is due to the flow returning back down to the surface, the flux tube would have to bend over a short distance and at least as quickly as appears to be the case for the inner footpoint. Flux pumping (Thomas et al. 2002) may provide the physical mechanism. However, Spruit & Scharmer (2006) argue that flux-pumping mechanism is inconsistent with observations, since it only operates at the outer penumbral boundary and not within the penumbra.

We further note that as the inner footpoint moves toward the inner penumbra, the outer edge of the flow (sharp boundary) initially stays in place (Figs. 7 and 10), but then also begins to move inward (see Fig. 9). If the sharp boundary marks the onset of the return flow, this would indicate that the outer footpoint, where the downflow occurs, moves inward as well. If the sharp edge marks the point where the flow enters into the canopy instead, as was suggested by Schlichenmaier et al. (1998a, 1998b), it does so in many cases well within the penumbra. More recent simulation results of the moving tube model (Schlichenmaier 2002) produce flux tubes that during the course of their evolution develop sea-serpent–like waves. This structure produces downflow arches well within the penumbra. However, we do not see any direct evidence for such sea-serpent-like flow structures in our data.

Infrared polarimetric observations of penumbral fine structure using two-component inversion techniques have provided strong evidence for the picture of an uncombed penumbra, where the penumbra is composed of a penumbral flux tube embedded in a magnetic background field (Borrero et al. 2004). The authors study a portion of the limb-side penumbra, as we did in this paper, and find that the Evershed effect is confined to the nearly horizontal flux tube component, while the background is essentially at rest. The bottom right panel of Figure 4 of Borrero et al. (2004) plots the inferred velocity as a function of penumbral radius for the flux tube and the background component. The flux tube component shows positive velocity throughout the penumbra, consistent with a horizontal outflow that is only slightly inclined in the inner penumbra. The background field is at rest only in the outer penumbra, while in the inner penumbra the inversion returns negative velocities (upflow). However, our observations clearly indicate that upflow occurs in the flux tube component at their inner footpoints. We note that the upflow derived for the background component from the inversion is very similar to the upflows we observe at the filament footpoints (order 1 km s^{-1}).

In order to understand this apparent discrepancy we have to keep in mind that vector magnetic field measurements often suffer from a lack of spatial resolution (Martínez Pillet 2000). This is in particular true for infrared observations such as the ones by Borrero et al. (2004). In fact, this is the primary reason for deploying multicomponent inversion techniques. However, uniqueness of the solution is often a question, and the interpretation is often difficult compared to observations in which the structures are resolved. Borrero et al. (2004) estimate the achieved spatial resolution to be about $1''$. At this resolution upflows with spatial extent $0\farcs2$–$0\farcs5$ and horizontal outflows are definitely mixed together in 1 pixel. It appears that the two-component inversion associates the upflows with the background component and the horizontal flows with the flux tube component even though according to our data they are part of the same flow along a flux tube.

Our observations have provided important new information that will help to distinguish between various existing penumbral models and hopefully will lead to more refined penumbra models. In the future we will attempt to confirm our observations and extend them by obtaining simultaneous high-resolution vector magnetic field measurements that are now possible with instruments such as the Diffraction-Limited Spectro-Polarimeter (DLSP). The DLSP is fed by a high-order adaptive optics corrected beam and can deliver $0\farcs2$ resolution vector polarimetric data. The DLSP can be combined with the UBF and high-resolution g-band speckle imaging, which might provide additional important information.

We are grateful to the technical and observing staff of the DST for their competent support. In part this work was supported by the National Science Foundation under grant 0079482.

Facilities: Dunn

REFERENCES

Beckers, J. M., & Schröter, E. H. 1969, Sol. Phys., 10, 384
Bellot Rubio, L. R., Balthasar, H., Collados, M., & Schlichenmaier, R. 2003, A&A, 403, L47
Bellot Rubio, L. R., Langhans, K., & Schlichenmaier, R. 2005, A&A, 443, L7
Borrero, J. M., Solanki, S. K., Bellot Rubio, L. R., Lagg, A., & Mathew, S. K. 2004, A&A, 422, 1093
Bruls, J. H. M. J., Lites, B. W., &, Murphy, G. A. 1991, in Solar Polarimetry, ed. L. J. November, 444
Evershed, J. 1909, Observatory, 32, 291
Grossmann-Doerth, U., Schmidt, W., & Schroeter, E. H. 1986, A&A, 156, 347
Hartkorn, K., & Rimmele, T. 2003, ASP Conf. Ser. 286, Current Theoretical Models and Future High Resolution Solar Observations, ed. A. A. Peterson & H. Uinterbroek (San Fransisco: ASP), 281
Langhans, K., Scharmer, G. B., Kiselman, D., Löfdahl, M. G., & Berger, T. E. 2005, A&A, 436, 1087
Lites, B. W., Elmore, D. F., Seagraves, P., & Skumanich, A. P. 1993, ApJ, 418, 928
Lites, B. W., Skumanich, A., & Scharmer, G. B. 1990, ApJ, 355, 329
Marino, J., Rimmele, T. R., & Christou, J. C. 2004, Proc. SPIE, 5490, 184
Martínez Pillet, V. 2000, A&A, 361, 734
Montesinos, B., & Thomas, J. H. 1997, Nature, 390, 485
———. 1998, Ap&SS, 263, 323
Rimmele, T. R. 1994, A&A, 290, 972
———. 1995a, A&A, 298, 260
———. 1995b, ApJ, 445, 511
———. 2004a, ApJ, 604, 906
———. 2004b, Proc. SPIE, 5490, 34
Scharmer, G. B., Gudiksen, B. V., Kiselman, D., Löfdahl, M. G., & Rouppe van der Voort, L. H. M. 2002, Nature, 420, 151
Schlichenmaier, R. 2002, Astron. Nachr., 323, 303
Schlichenmaier, R., Bellot Rubio, L. R., & Tritschler, A. 2004, A&A, 415, 731
———. 2005, Astron. Nachr., 326, 301
Schlichenmaier, R., Jahn, K., & Schmidt, H. U. 1998a, A&A, 337, 897
———. 1998b, ApJ, 493, L121
Schlichenmaier, R., & Solanki, S. K. 2003, A&A, 411, 257
Shine, R. A., Title, A. M., Tarbell, T. D., Smith, K., Frank, Z. A., & Scharmer, G. 1994, ApJ, 430, 413
Sobotka, M., Sütterlin, P. 2001, A&A, 380, 714
Solanki, S. K. 1993, Space Sci. Rev., 63, 1
———. 2003, A&A Rev., 11, 153
Solanki, S. K., & Montavon, C. A. P. 1993, A&A, 275, 283
Spruit, H. C., & Scharmer, G. B. 2006, A&A, 447, 343
Stanchfield, D. C. H., Thomas, J. H., & Lites, B. W. 1997, ApJ, 477, 485
Sütterlin, P., Bellot Rubio, L. R., & Schlichenmaier, R. 2004, A&A, 424, 1049
Thomas, J. H., & Montesinos, B. 1993, ApJ, 407, 398
Thomas, J. H., & Weiss, N. O., ed. 1992, Sunspots: Theory and Observations (Dordrecht: Kluwer)
———. 2004, ARA&A, 42, 517
Thomas, J. H., Weiss, N. O., Tobias, S. M., & Brummell, N. H. 2002, Nature, 420, 390
Title, A. M., Frank, Z. A., Shine, R. A., Tarbell, T. D., T opka, K. P., Scharmer, G., & Schmidt, W. 1993, ApJ, 403, 780
Tritschler, A., et al. 2004, A&A, 415, 717
Weiss, N. O. 2006, in ASP Conf. Ser., Solar MHD: Theory and Observations, ed. J. Leibacher & H. Uitenbroek (San Fransisco: ASP), in press
Westendorp Plaza, C., del Toro Iniesta, J. C., Ruiz Cobo, B., Martinez Pillet, V., Lites, B. W., & Skumanich, A. 1997, Nature, 389, 47
Wiehr, E., & Stellmacher, G. 1989, A&A, 225, 528
Véran, J.-P., Rigaut, F., Maître, H., & Rouan, D. 1997, J. Opt. Soc. Am. A, 14, 3057